

Lattice QCD constraints on the critical point from an improved precision equation of state

Szabolcs Borsányi,¹ Zoltán Fodor,^{2,3,1,4,5} Jana N. Guenther,¹ Paolo Parotto,⁶
Attila Pásztor,⁴ Claudia Ratti,⁷ Volodymyr Vovchenko,⁷ and Chik Him Wong¹

¹*University of Wuppertal, Department of Physics, Wuppertal D-42119, Germany*

²*Pennsylvania State University, Department of Physics, State College, PA 16801, USA*

³*Pennsylvania State University, Institute for Computational and Data Sciences, State College, PA 16801, USA*

⁴*Institute for Theoretical Physics, ELTE Eötvös Loránd University,
Pázmány P. sétány 1/A, H-1117 Budapest, Hungary*

⁵*Jülich Supercomputing Centre, Forschungszentrum Jülich, D-52425 Jülich, Germany*

⁶*Dipartimento di Fisica, Università di Torino and INFN Torino, Via P. Giuria 1, I-10125 Torino, Italy*

⁷*Department of Physics, University of Houston, Houston, TX 77204, USA*

(Dated: February 17, 2025)

In this Letter we employ lattice simulations to search for the critical point of quantum chromodynamics (QCD). We search for the onset of a first order QCD transition on the phase diagram by following contours of constant entropy density from imaginary to real chemical potentials under conditions of strangeness neutrality. We scan the phase diagram and investigate whether these contours meet to determine the probability that the critical point is located in a certain region on the $T - \mu_B$ plane. To achieve this we introduce a new, continuum extrapolated equation of state at zero density with improved precision using lattices with $N_\tau = 8, 10, 12, 16$ timeslices, and supplement it with new data at imaginary chemical potential. The current precision allows us to exclude, at the 2σ level, the existence of a critical point at $\mu_B < 450$ MeV.

INTRODUCTION

The study of the phase diagram of quantum chromodynamics (QCD) is an extremely active field of research, which encompasses conditions ranging from high energy heavy ion collisions to the mergers of neutron stars. The major tool for *ab initio* investigations of QCD thermodynamics are lattice simulations, which have shown that, at vanishing density, the transition separating the hadronic phase from the quark gluon plasma (QGP) is a broad crossover [1] located at around $T = 155 - 160$ MeV [2, 3].

At finite chemical potential μ_B , based on results from several effective approaches to QCD, it is conjectured that the crossover transition turns into a first order line at a critical endpoint (see e.g. [4, 5]). Lattice QCD at finite density suffers from a complex action problem, which renders simulations extremely costly. Several indirect approaches have been devised to circumvent this issue, most notably Taylor expansion around $\mu_B = 0$ [2, 6–14], analytic continuation from imaginary chemical potential [3, 12, 15–25] and reweighting techniques [26–37]. Results from these methods have been obtained for different quantities, like the equation of state, fluctuations of conserved charges or the QCD transition line, up to chemical potentials as large as $\mu_B \simeq 3.5T$, though no sign of criticality has been observed. Notable exceptions are attempts to extract the position of the corresponding Lee-Yang edge singularity from lattice data [14, 38–40].

The quest for the QCD critical point was one of the main motivations behind the extensive Beam Energy Scan program at the Relativistic Heavy Ion Collider, from which final results will come in the near future. Al-

though direct experimental evidence for the existence of a critical point is still missing, both the BES-I [41, 42] and preliminary BES-II results [43] on net-proton cumulants indicate deviations from non-critical baselines [44, 45] at the lowest energies, which might not be explainable without critical effects. At the moment, the uncertainties are still sizable, but more precise data and analysis in the future might clarify the issue.

Several recent predictions for the location of the critical point have been obtained via functional methods [46–51], holography [52–54] and the analysis of experimental data [55–58]. Many (but not all) of these predictions based on different approaches cluster in a rather small region on the QCD phase diagram. However, the systematic uncertainty of these approaches is hard to estimate. Hence, a method with controlled systematics is highly desirable.

In Ref. [64] a novel method, based solely on lattice results, was proposed to estimate the location of the critical point by studying contours of constant entropy density on the QCD phase diagram. The idea is to employ the entropy contours to search for the onset of a first order regime: if different contours meet somewhere in the phase diagram, it means that the entropy has become multi-valued, hence the transition has turned first order. By determining where the first order regime is reached, the location of the critical point can be estimated. In Ref. [64], the entropy contours were constructed based on existing lattice results at vanishing chemical potential for the entropy density [59] and second order baryon susceptibility [24].

In this work, we generalize this method in more than

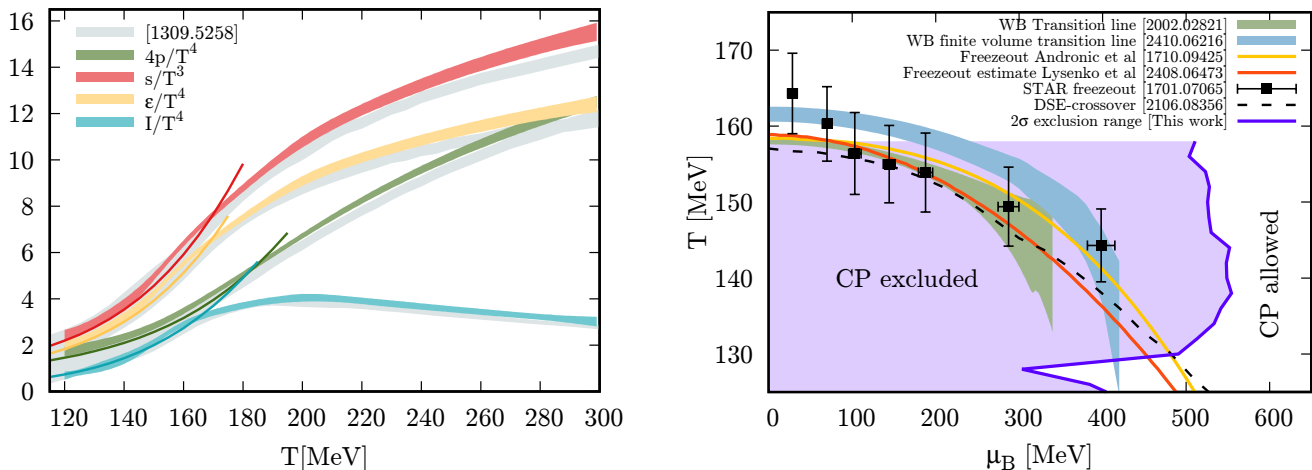


FIG. 1. Left: pressure (green), entropy (red), energy density (yellow) and trace anomaly (cyan) as functions of the temperature. The gray bands show our previous results from Ref. [59], while the curves at low temperature are due to the inclusion of the charm quark in our new results, as opposed to the 2+1 flavor result from Ref. [59]. Right: The QCD phase diagram in the $T - \mu_B$ plane with the 2σ exclusion range obtained in this work. We also show the chiral transition line from the continuum extrapolated lattice simulations in a large volume [3], as well as a recent result in a smaller system without continuum extrapolation [60] and a prediction based on Dyson-Schwinger equations [50]. Besides the STAR result for chemical freeze-out parameters for collision energies $\sqrt{s} = 200 - 7.7$ GeV [61] and its parametrization [62], we add a recent lower bound estimate based on a fixed energy/particle number ratio within the HRG framework [63].

one way. To reach the necessary precision to bear predictive power, we perform a new computation of the equation of state of QCD at zero density, with significantly reduced uncertainties compared to existing results. Instead of extracting the constant entropy contours from $\mu_B = 0$ data, we extrapolate them from imaginary μ_B . In addition, we increase the statistics of data sets at the three highest imaginary chemical potentials on the finest lattice in comparison to our earlier work [25]. While the extrapolation in Ref. [64] was done at order $\mathcal{O}(\mu_B^2)$, here we allow for leading corrections to the linear μ_B^2 dependence. We use the actual statistical correlations between variables and also consider additional sources of systematic errors in the analysis. Besides, the results presented in Ref. [64] were obtained for zero strangeness chemical potential, while here we enforce strangeness neutrality.

There are two main results in this Letter. We present an update of the zero-density equation of state (see tabulated data in the Supplemental Material). We also determine an exclusion probability for the existence of a critical point as a function of the chemical potential. We show both results in Fig. 1. We obtain our final result by combining our excluded region with the available information on the chemical freeze-out line [61–63]. To be conservative, we choose the curve in Ref. [63], which was estimated as a lower bound for the freeze-out temperature, and thus, also for T_c . We find that, at the 2σ level, we can exclude the existence of a critical point below $\mu_B^{2\sigma} = 450$ MeV.

In the following, we discuss the ingredients that have

led us to this finding. We first introduce the update to the zero-density equation of state [59] at $\mu_B = 0$ in the temperature range $T = 120 - 300$ MeV. We extend the entropy function to imaginary μ_B by continuum extrapolating the imaginary baryon density and its temperature derivative at these μ_B , maintaining strangeness neutrality. Finally, the contours of constant entropy are extrapolated to $\mu_B > 0$, and we calculate the probability for the entropy to be multi-valued at each point on the phase diagram,

EQUATION OF STATE AT $\mu_B = 0$

Throughout the analysis, we employ our 4stout staggered action with $N_f = 2+1+1$ quarks at physical quark masses. Thus, we compute the QCD pressure including the dynamical contribution of the charm quark. In Ref. [65] we already computed the equation of state with this lattice action at high temperatures, now we complement this to the transition region. Here the charm quark plays an insignificant role except for high temperatures, $T \gtrsim 250$ MeV. Methodically, we proceed as in Ref. [59], where the 2+1 flavor equation of state was computed earlier by us.

To determine the equation of state at vanishing chemical potential, we employ the integral method of Ref. [66], whereby the pressure is obtained through the integration

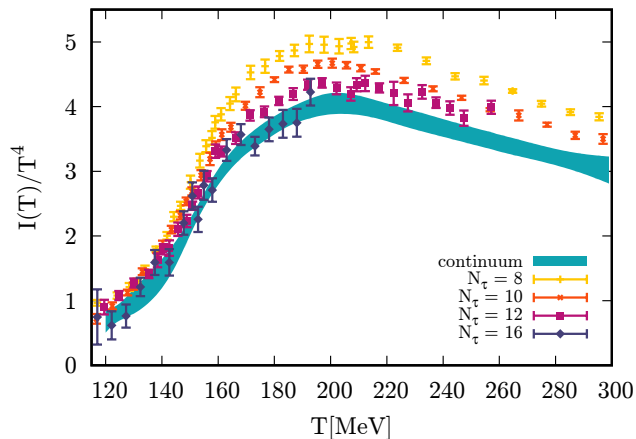


FIG. 2. Trace anomaly in the continuum (cyan band), as well as at finite N_τ (colored points).

of the trace anomaly:

$$\frac{p(T)}{T^4} = \frac{p(T_0)}{T_0^4} + \int_{T_0}^T \frac{dT'}{T'} \frac{I(T')}{T'^4}, \quad (1)$$

where $\frac{p(T_0)}{T_0^4}$ is an integration constant.

The integration constant and the trace anomaly are addressed separately with designated lattice runs, both are extrapolated to the continuum limit. We do not use model-dependent input (such as hadron resonance gas) to fix the integration constant, or to constrain the continuum limit.

Equation (1) is a multi-dimensional line integral in the space of the bare parameters of the action – the gauge coupling $\beta = 6/g^2$ and the fermion masses m_f – along the line of constant physics $m_f(\beta)$. The bare parameters of this discretization have been documented in Ref. [67]. Throughout this work, we use physical quark masses on $N_t = 8, 10, 12, 16$ lattices.

The trace anomaly can be written as:

$$\frac{I(T)}{T^4} = -TN_\tau^4 \frac{d\beta}{dT} \left(\langle -s_G \rangle + \sum_f \frac{dm_f}{d\beta} \langle \bar{\psi}_f \psi_f \rangle \right) \quad (2)$$

where $d\beta/dT$ is given by the scale setting and the $dm_f/d\beta$ are given by the line of constant physics. The expectation values $\langle -s_G \rangle$ and $\langle \bar{\psi}_f \psi_f \rangle$ are the gauge action and the chiral condensates, respectively. Both quantities require additive renormalization, which is carried out by subtracting the vacuum contribution at the same bare parameters:

$$\langle -s_G \rangle = \langle -s_G \rangle_T - \langle -s_G \rangle_0, \quad (3)$$

$$\langle \bar{\psi}_f \psi_f \rangle = \langle \bar{\psi}_f \psi_f \rangle_T - \langle \bar{\psi}_f \psi_f \rangle_0. \quad (4)$$

We performed a large number of zero-temperature simulations to reduce the noise on the vacuum term in

Eq. (3), which is responsible for much of the error on the trace anomaly itself [68]. We determine the trace anomaly in the range $T = 120 - 300$ MeV by combining a linear continuum limit in $1/N_\tau^2$ with a spline fit in the temperature. Details on the statistics and the fit procedure can be found in the Supplemental Material. The continuum extrapolated trace anomaly is shown in Fig. 2, together with the results on individual lattices.

The integration constant in Eq. (1) is determined in a similar way, by integrating the chiral condensate in the fermion masses from infinity, where the pressure vanishes, down to the physical values. In practice, it is sufficient to start from the mass of the charm quark m_c , integrate the 3-flavour theory down to the strange quark mass m_s , then integrate the two-flavour theory down to the light quark mass m_l :

$$\begin{aligned} \frac{p(T_0)}{T_0^4} &= \int_{m_s}^{m_l} dm_2 \langle \bar{\psi}\psi \rangle_2(m_2) \\ &+ \int_{\infty}^{m_s} dm_3 \langle \bar{\psi}\psi \rangle_3(m_3). \end{aligned} \quad (5)$$

Here, the subscripts 2, 3 refer to the $N_f = 2, 3$ flavour theories, and the chiral condensates are the renormalized ones. In this work we choose to calculate this constant at $T_0 = 185$ MeV, to minimize the uncertainty on the equation of state in the transition region.

For the continuum extrapolation of $p(T_0)/T_0^4$ we include $N_\tau = 10, 12, 16$ lattices. Several sources of systematic uncertainties are considered, for a total of 32 analyses, which are then combined with the histogram method introduced in Ref. [69]. The final result is:

$$\frac{p(T_0 = 185 \text{ MeV})}{T_0^4} = 1.371(28), \quad (6)$$

where the quoted error includes both statistical and systematic uncertainties. The precision we reach is approximately a $2\times$ improvement over our previous result [59]. Details on the extrapolation and the systematic analyses can be found in the Supplemental Material.

With Eq. (1) we can now determine the pressure, and from it the other thermodynamic quantities. Trace anomaly, pressure, entropy and energy density are shown in the left panel of Fig. 1 as colored bands, together with our previous results from Ref. [59], shown as gray bands for comparison. The improved precision in both terms of Eq. (1) results in a substantial improvement for the precision of all quantities, especially near the transition region. Note that our previous results were obtained with $N_f = 2 + 1$ quarks: the contribution of the charm quark becomes non-negligible at around $T \simeq 250$ MeV.

ENTROPY CONTOURS

In this work we construct and follow contours of constant entropy density from imaginary to real baryon

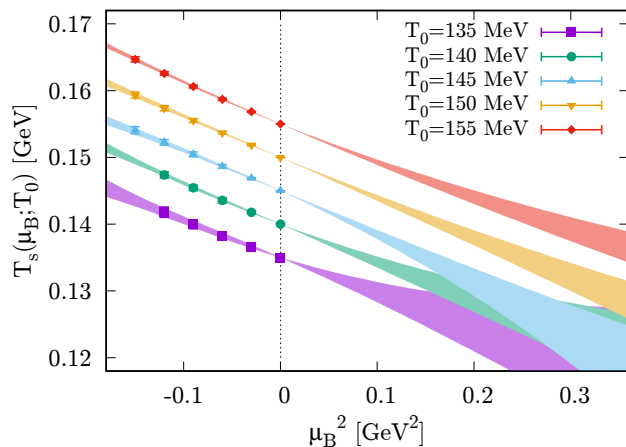


FIG. 3. Contours of constant (dimensionful) entropy density as fitted rational functions on continuum extrapolated lattice data. Each contour is labeled by its crossing point at $\mu_B = 0$: T_0 . Note that the extrapolation is defined in the dimensionful μ_B^2 (see also [64]), not μ_B/T .

chemical potential. These contours are defined at vanishing strangeness density and zero electric charge chemical potential. At finite (real or imaginary) μ_B , the entropy density can be written as:

$$s(T, \mu_B) = s(T, \mu_B = 0) + \int_0^{\mu_B} d\mu'_B \frac{\partial n_B(T, \mu'_B)}{\partial T}, \quad (7)$$

where the first term comes from the continuum extrapolated equation of state discussed in the previous section, and $n_B(T, \mu_B)$ is the baryon density. We construct a continuum extrapolation of $n_B(T, \mu_B)$ for imaginary values of the chemical potential μ_B by employing simulations at imaginary chemical potentials on lattices with $N_\tau = 10, 12$ and 16 timeslices. We perform a combined fit in the temperature T , the baryochemical potential μ_B and the lattice spacing $1/N_\tau^2$. Details on the fit and the systematic analyses can be found in the Supplemental Material.

From the continuum extrapolated baryon density we construct the entropy density at imaginary chemical potential using Eq. (7). In order to construct the contours, we proceed as follows. For each temperature T_0 , we first calculate the corresponding value $s(T_0)$ of the entropy at $\mu_B = 0$. For each chemical potential, we then determine the temperature $T_s(\mu_B, T_0)$ at which the entropy has the desired value $s(T_0)$. The function $T_s(\mu_B, T_0)$ then yields the contour stemming from T_0 . By repeating the procedure for several values of T_0 , we obtain the contours shown as points in Fig. 3 for $\mu_B^2 < 0$. We observe that the dependence of $T_s(T_0, \mu_B)$ on μ_B^2 is remarkably linear to a high precision. In order to account for deviations from an exact linear behavior, we consider an extrapolation to real chemical potential based on a rational ansatz

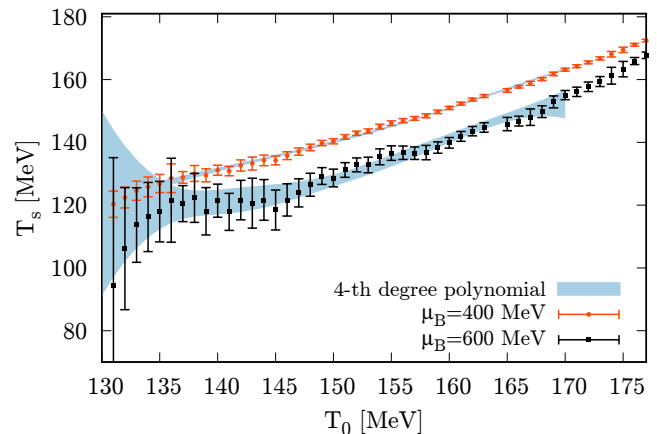


FIG. 4. The value of $T_s(\mu_B^2, T_0)$ for two fixed values of the baryochemical potential. These curves develop a negative derivative in the first order regime, and an exactly vanishing derivative at the critical point.

of the form:

$$T_s(\mu_B^2, T_0) = \frac{T_0 + a\mu_B^2}{1 + b\mu_B^2}. \quad (8)$$

The results are shown as bands in Fig. 3.

In order to determine the onset of a first order transition regime on the phase diagram, we now study the contours $T_s(\mu_B^2, T_0)$ for different, fixed values of μ_B . Because the entropy is a monotonic function of the temperature in the absence of a discontinuity, the curve $T_s(\mu_B^2, T_0)$ will be, at fixed μ_B , monotonic as well. However, if and when the entropy develops a discontinuity, there will be a regime where the derivative $(\partial T_s / \partial T_0)_{\mu_B}$ drops below zero, while being exactly zero at the critical point. We can see a pattern similar to the expected one in Fig. 4, where $T_s(\mu_B^2, T_0)$ is shown for two values of μ_B . At large chemical potentials data are consistent with a zero or negative derivative within some level of confidence (e.g. $\mu_B = 600$ MeV in Fig. 4).

We identify this confidence level for each $T - \mu_B$ pair in the phase diagram. First, we solve $T = T_s(\mu_B^2, T_0)$ for T_0 , and then evaluate $(\partial T_s / \partial T_0)_{\mu_B}$ at that value. For a broad range of parameters, this is at least one or two σ larger than zero, indicating that at the given $T - \mu_B$ position, the entropy is not multi-valued to the given level of confidence.

We exemplify this in the top panel of Fig. 5. The two curves represent two horizontal stripes in the phase diagram, where this analysis was carried out. The plot shows the levels that would belong to 1σ and 2σ around the central value, if the distribution was Gaussian. We translate this to a confidence level in the bottom panel. There we also show the probability of having a negative slope of $T_s(T_0)$ along two versions of the chemical freeze-out line [62, 63] and a prediction of the cross-over line

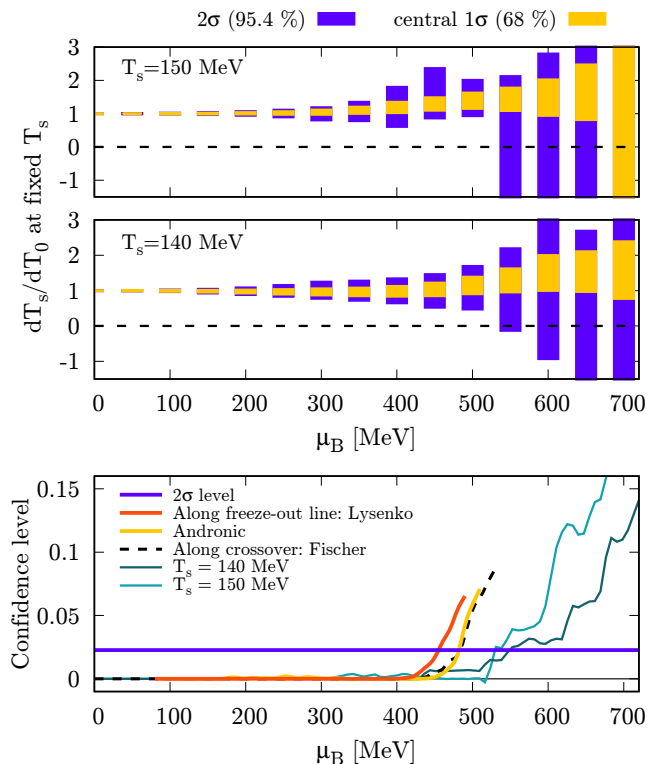


FIG. 5. Top: the derivative of the $T_s(T_0)$ curve at fixed chemical potential as a function of T_0 (see Fig. 4). This quantity is positive for a crossover, negative for a first order transition and zero at the critical point. Bottom: the confidence level for the $(\partial T_s/\partial T_0)_{\mu_B} < 0$ hypothesis for two fixed values of T_s and along the predicted crossover line of Ref. [50]. We also show the confidence levels along the two freeze-out lines in Fig. 1.

[50] in the phase diagram.

The data in Fig. 5 already refer to the full systematic analysis. In particular, we performed 16 different continuum extrapolations to arrive at the entropy at imaginary μ_B , and once extrapolated to $\mu_B > 0$, each resulting T_s function was interpolated in 12 different ways. Though each of the $12 \cdot 16 = 192$ such analyses provides a Gaussian statistical error, once their respective cumulative distribution function is averaged, the result is non-Gaussian. The main result in Fig. 1 shows the chemical potential for a set of fixed temperatures where the confidence level reaches 0.02275 for 2σ . At the 2σ confidence level the lower bound is $\mu_B^{2\sigma} = 450$ MeV.

CONCLUSIONS

We presented an update of the QCD equation of state at $\mu_B = 0$ with improved precision in comparison to our previous result [59]. This result was obtained with the (2+1+1 flavor) 4stout staggered action up to a resolution of $N_\tau = 16$ to perform a continuum extrapolation.

This allowed us to calculate contours of constant entropy on the QCD phase diagram in the $T - \mu_B$ plane, by analytic continuation from purely imaginary chemical potentials using continuum extrapolated lattice QCD simulations in a large volume: $LT = 4$ in temperature units. Unlike previous estimates based on lattice simulations, we show results on the phenomenologically relevant strangeness neutral line. The contours of constant entropy in principle allow one to locate the spinodal region, and thus the onset of a first order transition at the coveted critical endpoint. While some of the considered analyses indeed show a critical endpoint, we have found that after taking into account all systematic and statistical uncertainties, the location of the critical endpoint cannot be unambiguously bracketed. This also means that our analysis does not provide a clear proof of the existence of such a critical endpoint. However - for the first time in the literature - we are able to give reliable lower bounds on the critical endpoint location in continuum QCD.

Supplementing the analysis with the known heavy-ion chemical freeze-out line (Fig. 1), we can exclude the existence of the critical point, at the 2σ level, below $\mu_B^{2\sigma} = 450$ MeV. Our results for the critical endpoint are consistent with the conclusions from an analysis of the Polyakov loop in a small physical volume in Ref. [60], where a broadening of the crossover transition was observed at $\mu_B \lesssim 400$ MeV.

From chiral effective models one expects the transition temperature in the chiral limit at zero density to be an upper bound for the critical point at finite density [70]. The $O(4)$ critical temperature in the chiral limit was recently calculated to be $T_\chi \sim 133$ MeV [71, 72]. Translating our lower bound on the critical chemical potential to an upper bound in temperature, our finding is consistent with the above expectation.

Acknowledgments - This work is supported by the MKW NRW under the funding code NW21-024-A. Further funding was received from the DFG under the Project No. 496127839. This work was also supported by the Hungarian National Research, Development and Innovation Office, NKFIH Grant No. KKP126769. This work was also supported by the NKFIH excellence grant TKP2021_NKTA_64. This work is also supported by the Hungarian National Research, Development and Innovation Office under Project No. FK 147164. This material is also based upon work supported by the National Science Foundation under grants No. PHY-2208724, and PHY-2116686, and within the framework of the MUSES collaboration, under grant number No. OAC-2103680. This material is also based upon work supported by the U.S. Department of Energy, Office of Science, Office of Nuclear Physics, under Award Numbers DE-SC0022023 and DE-SC0025025, as well as by the National Aeronautics and Space Agency (NASA) under

Award Number 80NSSC24K0767. The authors gratefully acknowledge the Gauss Centre for Supercomputing e.V. (www.gauss-centre.eu) for funding this project by providing computing time on the GCS Supercomputer HAWK at HLRS, Stuttgart. An award of computer time was provided by the INCITE program. This research used resources of the Argonne Leadership Computing Facility, which is a DOE Office of Science User Facility supported under Contract DE-AC02-06CH11357.

-
- [1] Y. Aoki, G. Endrodi, Z. Fodor, S. D. Katz, and K. K. Szabo, The Order of the quantum chromodynamics transition predicted by the standard model of particle physics, *Nature* **443**, 675 (2006), arXiv:hep-lat/0611014 [hep-lat].
- [2] A. Bazavov *et al.* (HotQCD), Chiral crossover in QCD at zero and non-zero chemical potentials, *Phys. Lett. B* **795**, 15 (2019), arXiv:1812.08235 [hep-lat].
- [3] S. Borsanyi, Z. Fodor, J. N. Guenther, R. Kara, S. D. Katz, P. Parotto, A. Pasztor, C. Ratti, and K. K. Szabo, QCD Crossover at Finite Chemical Potential from Lattice Simulations, *Phys. Rev. Lett.* **125**, 052001 (2020), arXiv:2002.02821 [hep-lat].
- [4] A. Bzdak, S. Esumi, V. Koch, J. Liao, M. Stephanov, and N. Xu, Mapping the Phases of Quantum Chromodynamics with Beam Energy Scan, *Phys. Rept.* **853**, 1 (2020), arXiv:1906.00936 [nucl-th].
- [5] L. Du, A. Sorensen, and M. Stephanov, The QCD phase diagram and Beam Energy Scan physics: a theory overview, *Int. J. Mod. Phys. E* **33**, 2430008 (2024), arXiv:2402.10183 [nucl-th].
- [6] C. R. Allton, S. Ejiri, S. J. Hands, O. Kaczmarek, F. Karsch, E. Laermann, and C. Schmidt, The Equation of state for two flavor QCD at nonzero chemical potential, *Phys. Rev. D* **68**, 014507 (2003), arXiv:hep-lat/0305007.
- [7] C. R. Allton, M. Doring, S. Ejiri, S. J. Hands, O. Kaczmarek, F. Karsch, E. Laermann, and K. Redlich, Thermodynamics of two flavor QCD to sixth order in quark chemical potential, *Phys. Rev. D* **71**, 054508 (2005), arXiv:hep-lat/0501030 [hep-lat].
- [8] O. Kaczmarek, F. Karsch, E. Laermann, C. Miao, S. Mukherjee, P. Petreczky, C. Schmidt, W. Soeldner, and W. Unger, Phase boundary for the chiral transition in (2+1) -flavor QCD at small values of the chemical potential, *Phys. Rev. D* **83**, 014504 (2011), arXiv:1011.3130 [hep-lat].
- [9] G. Endrodi, Z. Fodor, S. D. Katz, and K. K. Szabo, The QCD phase diagram at nonzero quark density, *JHEP* **04**, 001, arXiv:1102.1356 [hep-lat].
- [10] S. Borsanyi, G. Endrodi, Z. Fodor, S. D. Katz, S. Krieg, C. Ratti, and K. K. Szabo, QCD equation of state at nonzero chemical potential: continuum results with physical quark masses at order mu^2 , *JHEP* **08**, 053, arXiv:1204.6710 [hep-lat].
- [11] A. Bazavov *et al.*, The QCD Equation of State to $\mathcal{O}(\mu_B^6)$ from Lattice QCD, *Phys. Rev. D* **95**, 054504 (2017), arXiv:1701.04325 [hep-lat].
- [12] C. Bonati, M. D'Elia, F. Negro, F. Sanfilippo, and K. Zambello, Curvature of the pseudocritical line in QCD: Taylor expansion matches analytic continuation, *Phys. Rev. D* **98**, 054510 (2018), arXiv:1805.02960 [hep-lat].
- [13] A. Bazavov *et al.* (HotQCD), Chiral crossover in QCD at zero and non-zero chemical potentials, *Phys. Lett. B* **795**, 15 (2019), arXiv:1812.08235 [hep-lat].
- [14] D. Bollweg, J. Goswami, O. Kaczmarek, F. Karsch, S. Mukherjee, P. Petreczky, C. Schmidt, and P. Scior (HotQCD), Taylor expansions and Padé approximants for cumulants of conserved charge fluctuations at nonvanishing chemical potentials, *Phys. Rev. D* **105**, 074511 (2022), arXiv:2202.09184 [hep-lat].
- [15] P. de Forcrand and O. Philipsen, The QCD phase diagram for small densities from imaginary chemical potential, *Nucl. Phys. B* **642**, 290 (2002), arXiv:hep-lat/0205016 [hep-lat].
- [16] M. D'Elia and M.-P. Lombardo, Finite density QCD via imaginary chemical potential, *Phys. Rev. D* **67**, 014505 (2003), arXiv:hep-lat/0209146 [hep-lat].
- [17] M. D'Elia, F. Di Renzo, and M. P. Lombardo, The Strongly interacting quark gluon plasma, and the critical behaviour of QCD at imaginary μ , *Phys. Rev. D* **76**, 114509 (2007), arXiv:0705.3814 [hep-lat].
- [18] P. Cea, L. Cosmai, M. D'Elia, C. Manneschi, and A. Papa, Analytic continuation of the critical line: Suggestions for QCD, *Phys. Rev. D* **80**, 034501 (2009), arXiv:0905.1292 [hep-lat].
- [19] C. Bonati, M. D'Elia, M. Mariti, M. Mesiti, F. Negro, and F. Sanfilippo, Curvature of the chiral pseudocritical line in QCD: Continuum extrapolated results, *Phys. Rev. D* **92**, 054503 (2015), arXiv:1507.03571 [hep-lat].
- [20] P. Cea, L. Cosmai, and A. Papa, Critical line of 2+1 flavor QCD: Toward the continuum limit, *Phys. Rev. D* **93**, 014507 (2016), arXiv:1508.07599 [hep-lat].
- [21] R. Bellwied, S. Borsanyi, Z. Fodor, J. Guenther, S. D. Katz, C. Ratti, and K. K. Szabo, The QCD phase diagram from analytic continuation, *Phys. Lett. B* **751**, 559 (2015), arXiv:1507.07510 [hep-lat].
- [22] V. Vovchenko, A. Pasztor, Z. Fodor, S. D. Katz, and H. Stoecker, Repulsive baryonic interactions and lattice QCD observables at imaginary chemical potential, *Phys. Lett. B* **775**, 71 (2017), arXiv:1708.02852 [hep-ph].
- [23] V. Vovchenko, J. Steinheimer, O. Philipsen, and H. Stoecker, Cluster Expansion Model for QCD Baryon Number Fluctuations: No Phase Transition at $\mu_B/T < \pi$, *Phys. Rev. D* **97**, 114030 (2018), arXiv:1711.01261 [hep-ph].
- [24] S. Borsányi, Z. Fodor, J. N. Guenther, R. Kara, S. D. Katz, P. Parotto, A. Pásztor, C. Ratti, and K. K. Szabó, Lattice QCD equation of state at finite chemical potential from an alternative expansion scheme, *Phys. Rev. Lett.* **126**, 232001 (2021), arXiv:2102.06660 [hep-lat].
- [25] S. Borsanyi, J. N. Guenther, R. Kara, Z. Fodor, P. Parotto, A. Pasztor, C. Ratti, and K. K. Szabo, Resummed lattice QCD equation of state at finite baryon density: Strangeness neutrality and beyond, *Phys. Rev. D* **105**, 114504 (2022), arXiv:2202.05574 [hep-lat].
- [26] I. M. Barbour, S. E. Morrison, E. G. Klepfish, J. B. Kogut, and M.-P. Lombardo, Results on finite density QCD, *Nucl. Phys. B Proc. Suppl.* **60**, 220 (1998), arXiv:hep-lat/9705042.
- [27] Z. Fodor and S. D. Katz, A New method to study lattice QCD at finite temperature and chemical potential, *Phys. Lett. B* **534**, 87 (2002), arXiv:hep-lat/0104001 [hep-lat].
- [28] Z. Fodor and S. D. Katz, Lattice determination of the

- critical point of QCD at finite T and μ , *JHEP* **03**, 014, arXiv:hep-lat/0106002 [hep-lat].
- [29] Z. Fodor and S. D. Katz, Critical point of QCD at finite T and μ , lattice results for physical quark masses, *JHEP* **04**, 050, arXiv:hep-lat/0402006 [hep-lat].
- [30] P. de Forcrand, S. Kim, and T. Takaishi, QCD simulations at small chemical potential, *Nucl. Phys. B Proc. Suppl.* **119**, 541 (2003), arXiv:hep-lat/0209126.
- [31] A. Alexandru, M. Faber, I. Horvath, and K.-F. Liu, Lattice QCD at finite density via a new canonical approach, *Phys. Rev. D* **72**, 114513 (2005), arXiv:hep-lat/0507020 [hep-lat].
- [32] Z. Fodor, S. D. Katz, and C. Schmidt, The Density of states method at non-zero chemical potential, *JHEP* **03**, 121, arXiv:hep-lat/0701022 [hep-lat].
- [33] G. Endrodi, Z. Fodor, S. D. Katz, D. Sexty, K. K. Szabo, and C. Torok, Applying constrained simulations for low temperature lattice QCD at finite baryon chemical potential, *Phys. Rev. D* **98**, 074508 (2018), arXiv:1807.08326 [hep-lat].
- [34] M. Giordano, K. Kapas, S. D. Katz, D. Negradi, and A. Pasztor, Effect of stout smearing on the phase diagram from multiparameter reweighting in lattice QCD, *Phys. Rev. D* **102**, 034503 (2020), arXiv:2003.04355 [hep-lat].
- [35] M. Giordano, K. Kapas, S. D. Katz, D. Negradi, and A. Pasztor, New approach to lattice QCD at finite density; results for the critical end point on coarse lattices, *JHEP* **05**, 088, arXiv:2004.10800 [hep-lat].
- [36] S. Borsanyi, Z. Fodor, M. Giordano, S. D. Katz, D. Negradi, A. Pasztor, and C. H. Wong, Lattice simulations of the QCD chiral transition at real baryon density, *Phys. Rev. D* **105**, L051506 (2022), arXiv:2108.09213 [hep-lat].
- [37] S. Borsanyi, Z. Fodor, M. Giordano, J. N. Guenther, S. D. Katz, A. Pasztor, and C. H. Wong, Equation of state of a hot-and-dense quark gluon plasma: Lattice simulations at real μ_B vs extrapolations, *Phys. Rev. D* **107**, L091503 (2023), arXiv:2208.05398 [hep-lat].
- [38] G. Basar, QCD critical point, Lee-Yang edge singularities, and Padé resummations, *Phys. Rev. C* **110**, 015203 (2024), arXiv:2312.06952 [hep-th].
- [39] D. A. Clarke, P. Dimopoulos, F. Di Renzo, J. Goswami, C. Schmidt, S. Singh, and K. Zambello, Searching for the QCD critical endpoint using multi-point Padé approximations, (2024), arXiv:2405.10196 [hep-lat].
- [40] A. Adam, S. Borsányi, Z. Fodor, J. N. Guenther, P. Parotto, A. Pásztor, D. Pesznyák, L. Pirelli, and C. H. Wong, Search for a Lee-Yang edge singularity in high-statistics Wuppertal-Budapest data, in *41st International Symposium on Lattice Field Theory* (2025) arXiv:2502.03211 [hep-lat].
- [41] J. Adam *et al.* (STAR), Nonmonotonic Energy Dependence of Net-Proton Number Fluctuations, *Phys. Rev. Lett.* **126**, 092301 (2021), arXiv:2001.02852 [nucl-ex].
- [42] M. Abdallah *et al.* (STAR), Cumulants and correlation functions of net-proton, proton, and antiproton multiplicities distributions in Au+Au collisions at energies available at the BNL Relativistic Heavy Ion Collider, *Phys. Rev. C* **104**, 024902 (2021), arXiv:2101.12413 [nucl-ex].
- [43] A. Pandav, Precision measurement of net-proton number fluctuations in Au+Au collisions at RHIC (2024), Talk given at Critical Point and Onset of Deconfinement (CPOD) 2024.
- [44] P. Braun-Munzinger, B. Friman, K. Redlich, A. Rustamov, and J. Stachel, Relativistic nuclear collisions: Establishing the non-critical baseline for fluctuation measurements, (2020), arXiv:2007.02463 [nucl-th].
- [45] V. Vovchenko, V. Koch, and C. Shen, Proton number cumulants and correlation functions in Au-Au collisions at $s_{NN}=7.7-200$ GeV from hydrodynamics, *Phys. Rev. C* **105**, 014904 (2022), arXiv:2107.00163 [hep-ph].
- [46] P. Isserstedt, M. Buballa, C. S. Fischer, and P. J. Gunkel, Baryon number fluctuations in the QCD phase diagram from Dyson-Schwinger equations, *Phys. Rev. D* **100**, 074011 (2019), arXiv:1906.11644 [hep-ph].
- [47] W.-j. Fu, J. M. Pawłowski, and F. Rennecke, QCD phase structure at finite temperature and density, *Phys. Rev. D* **101**, 054032 (2020), arXiv:1909.02991 [hep-ph].
- [48] F. Gao and J. M. Pawłowski, Chiral phase structure and critical end point in QCD, *Phys. Lett. B* **820**, 136584 (2021), arXiv:2010.13705 [hep-ph].
- [49] F. Gao and J. M. Pawłowski, QCD phase structure from functional methods, *Phys. Rev. D* **102**, 034027 (2020), arXiv:2002.07500 [hep-ph].
- [50] P. J. Gunkel and C. S. Fischer, Locating the critical end-point of QCD: Mesonic backcoupling effects, *Phys. Rev. D* **104**, 054022 (2021), arXiv:2106.08356 [hep-ph].
- [51] W.-j. Fu, X. Luo, J. M. Pawłowski, F. Rennecke, R. Wen, and S. Yin, Hyper-order baryon number fluctuations at finite temperature and density, *Phys. Rev. D* **104**, 094047 (2021), arXiv:2101.06035 [hep-ph].
- [52] R. Critelli, J. Noronha, J. Noronha-Hostler, I. Portillo, C. Ratti, and R. Rougemont, Critical point in the phase diagram of primordial quark-gluon matter from black hole physics, *Phys. Rev. D* **96**, 096026 (2017), arXiv:1706.00455 [nucl-th].
- [53] M. Hippert, J. Grefa, T. A. Manning, J. Noronha, J. Noronha-Hostler, I. Portillo Vazquez, C. Ratti, R. Rougemont, and M. Trujillo, Bayesian location of the QCD critical point from a holographic perspective, *Phys. Rev. D* **110**, 094006 (2024), arXiv:2309.00579 [nucl-th].
- [54] L. Zhu, X. Chen, K. Zhou, H. Zhang, and M. Huang, Bayesian Inference of the Critical Endpoint in 2+1-Flavor System from Holographic QCD, (2025), arXiv:2501.17763 [hep-ph].
- [55] E. S. Fraga, L. F. Palhares, and P. Sorensen, Finite-size scaling as a tool in the search for the QCD critical point in heavy ion data, *Phys. Rev. C* **84**, 011903 (2011), arXiv:1104.3755 [hep-ph].
- [56] R. A. Lacey, Indications for a critical point in the phase diagram for hot and dense nuclear matter, *Nucl. Phys. A* **956**, 348 (2016), arXiv:1512.09152 [nucl-ex].
- [57] A. Sorensen and P. Sorensen, Locating the critical point for the hadron to quark-gluon plasma phase transition from finite-size scaling of proton cumulants in heavy-ion collisions, (2024), arXiv:2405.10278 [nucl-th].
- [58] J. Steinheimer, M. Omana Kuttan, T. Reichert, Y. Nara, and M. Bleicher, Predicting the QCD critical point and EoS from combining HIC and neutron star observations, (2025), arXiv:2501.12849 [hep-ph].
- [59] S. Borsanyi, Z. Fodor, C. Hoelbling, S. D. Katz, S. Krieg, and K. K. Szabo, Full result for the QCD equation of state with 2+1 flavors, *Phys. Lett. B* **730**, 99 (2014), arXiv:1309.5258 [hep-lat].
- [60] S. Borsanyi, Z. Fodor, J. N. Guenther, P. Parotto, A. Pasztor, L. Pirelli, K. K. Szabo, and C. H. Wong, QCD deconfinement transition line up to $\mu_B=400$ MeV from finite volume lattice simulations, *Phys. Rev. D* **110**, 114507 (2024), arXiv:2410.06216 [hep-lat].

- [61] L. Adamczyk *et al.* (STAR), Bulk Properties of the Medium Produced in Relativistic Heavy-Ion Collisions from the Beam Energy Scan Program, *Phys. Rev. C* **96**, 044904 (2017), arXiv:1701.07065 [nucl-ex].
- [62] A. Andronic, P. Braun-Munzinger, K. Redlich, and J. Stachel, Decoding the phase structure of QCD via particle production at high energy, *Nature* **561**, 321 (2018), arXiv:1710.09425 [nucl-th].
- [63] A. Lysenko, M. I. Gorenstein, R. Poberezhniuk, and V. Vovchenko, Chemical freeze-out curve in heavy-ion collisions and the QCD critical point, (2024), arXiv:2408.06473 [nucl-th].
- [64] H. Shah, M. Hippert, J. Noronha, C. Ratti, and V. Vovchenko, Locating the QCD critical point from first principles through contours of constant entropy density, (2024), arXiv:2410.16206 [hep-ph].
- [65] S. Borsanyi *et al.*, Calculation of the axion mass based on high-temperature lattice quantum chromodynamics, *Nature* **539**, 69 (2016), arXiv:1606.07494 [hep-lat].
- [66] J. Engels, J. Fingberg, F. Karsch, D. Miller, and M. Weber, Nonperturbative thermodynamics of SU(N) gauge theories, *Phys. Lett. B* **252**, 625 (1990).
- [67] R. Bellwied, S. Borsanyi, Z. Fodor, S. D. Katz, A. Pasztor, C. Ratti, and K. K. Szabo, Fluctuations and correlations in high temperature QCD, *Phys. Rev. D* **92**, 114505 (2015), arXiv:1507.04627 [hep-lat].
- [68] S. Borsanyi, G. Endrodi, Z. Fodor, A. Jakovac, S. D. Katz, S. Krieg, C. Ratti, and K. K. Szabo, The QCD equation of state with dynamical quarks, *JHEP* **11**, 077, arXiv:1007.2580 [hep-lat].
- [69] S. Borsanyi *et al.*, Leading hadronic contribution to the muon magnetic moment from lattice QCD, *Nature* **593**, 51 (2021), arXiv:2002.12347 [hep-lat].
- [70] A. M. Halasz, A. D. Jackson, R. E. Shrock, M. A. Stephanov, and J. J. M. Verbaarschot, On the phase diagram of QCD, *Phys. Rev. D* **58**, 096007 (1998), arXiv:hep-ph/9804290 [hep-ph].
- [71] H. T. Ding *et al.* (HotQCD), Chiral Phase Transition Temperature in (2+1)-Flavor QCD, *Phys. Rev. Lett.* **123**, 062002 (2019), arXiv:1903.04801 [hep-lat].
- [72] A. Y. Kotov, M. P. Lombardo, and A. Trunin, QCD transition at the physical point, and its scaling window from twisted mass Wilson fermions, *Phys. Lett. B* **823**, 136749 (2021), arXiv:2105.09842 [hep-lat].
- [73] S. Borsányi, S. Dürr, Z. Fodor, C. Hoelbling, S. D. Katz, S. Krieg, T. Kurth, L. Lellouch, T. Lippert, and C. McNeile (BMW), High-precision scale setting in lattice QCD, *JHEP* **09**, 010, arXiv:1203.4469 [hep-lat].

Supplemental material

EQUATION OF STATE AT $\mu_B = 0$

Trace anomaly

We performed high-statistics simulations dedicated to the renormalization of the gauge action. We show in Fig. S1 the statistics we collected for the simulated values of β .

The trace anomaly is defined as:

$$\frac{I(T)}{T^4} = -TN_\tau^4 \frac{d\beta}{dT} \left(\langle -s_G \rangle + \sum_f \frac{dm_f}{d\beta} \langle \bar{\psi}_f \psi_f \rangle \right), \quad (\text{S1})$$

where $d\beta/dT$ is given by the scale setting and the $dm_f/d\beta$ are given by the line of constant physics. The expectation

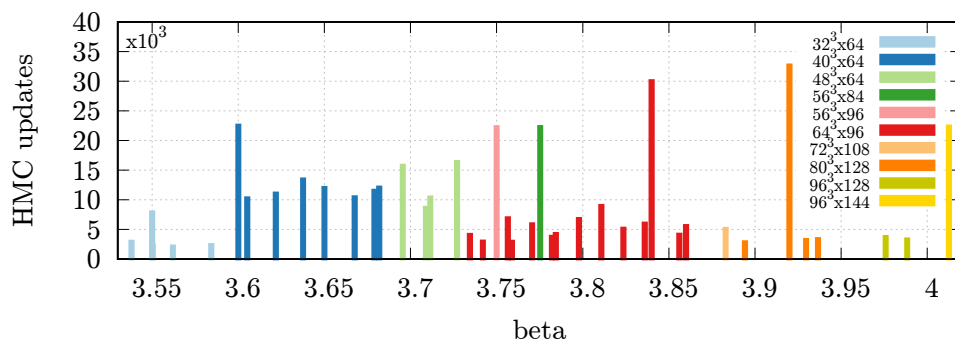


FIG. S1. Accumulated statistics for the vacuum runs used for renormalization. Different colors indicate different lattices.

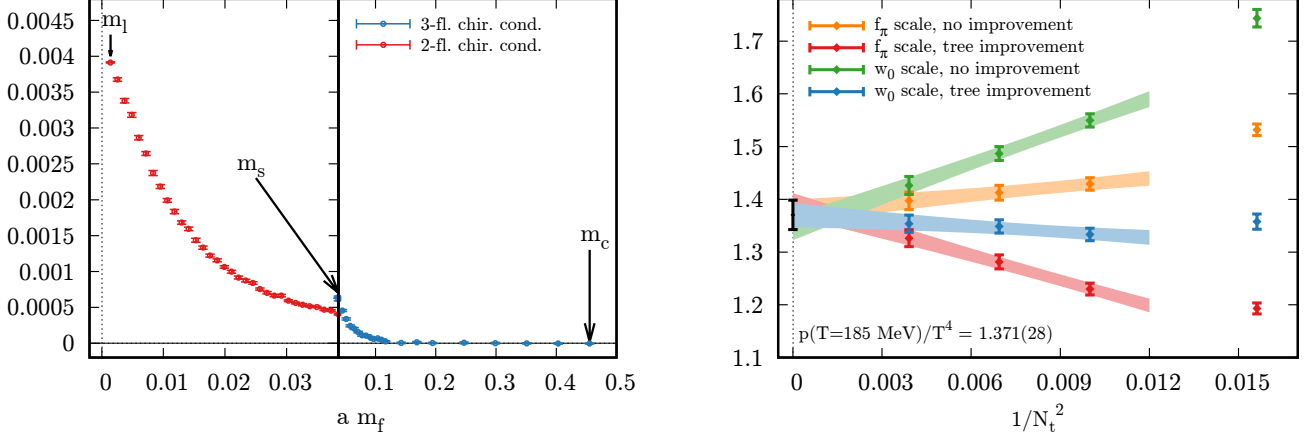


FIG. S2. Left: chiral condensate in the 2– and 3–flavour theories for quark masses between the light m_l and charm m_c values. Right: continuum limit of the pressure obtained directly at $T = 185$ MeV from Eq. (S9).

values $\langle -s_G \rangle$ and $\langle \bar{\psi}_f \psi_f \rangle$ are renormalized by subtracting the vacuum contribution at the same bare parameters:

$$\langle -s_G \rangle = \langle -s_G \rangle_T - \langle -s_G \rangle_0, \quad (\text{S2})$$

$$\langle \bar{\psi}_f \psi_f \rangle = \langle \bar{\psi}_f \psi_f \rangle_T - \langle \bar{\psi}_f \psi_f \rangle_0. \quad (\text{S3})$$

In order to determine the continuum limit of $I(T)$, we employ a procedure whereby we separately fit the vacuum gauge action, and the fixed- N_τ trace anomaly *minus* the aforementioned vacuum gauge action.

For the first fit, the chi square reads:

$$\chi_0^2 = \sum_{m \in \Lambda_0} \frac{\left(\sum_{a=0}^d \alpha_a \beta^a - \langle -s_g \rangle_0 \right)^2}{\sigma_m^2}, \quad (\text{S4})$$

where the vacuum gauge action, common to all lattices, is modeled with a polynomial of order d in β :

$$\langle -s_g \rangle_0 = \sum_{a=0}^d \alpha_a \beta^a, \quad (\text{S5})$$

and with σ_m^2 the errors on $\langle -s_g \rangle_0$.

For the second fit, the chi square reads:

$$\chi_T^2 = \sum_{n \in \Lambda_T} \frac{\left(\sum_{i \in K} S_i(T) \left(c_i + \frac{d_i}{N_\tau^2} \right) + TN_\tau^4 \frac{d\beta}{dT} \sum_{a=0}^d \alpha_a \beta^a - g_n \right)^2}{\sigma_n^2}, \quad (\text{S6})$$

where the fixed- N_τ trace anomaly *minus* the vacuum gauge action is:

$$g_n = TN_\tau^4 \left[\langle -s_g \rangle_T \frac{d\beta}{dT} + \sum_{f \in \text{flavours}} \langle \bar{\psi}_f \psi_f \rangle \frac{dm_f}{dT} \right], \quad (\text{S7})$$

with σ_n^2 the errors on g_n . We model this quantity with cubic splines $S_i(T)$ with nodes K , where each parameter is additionally a linear model in $1/N_\tau^2$.

We perform the global fit by minimizing the combined chi square:

$$\chi^2 = \chi_0^2 + \chi_T^2. \quad (\text{S8})$$

We consider several sources of systematic uncertainties:

- we set the scale with either f_π or w_0 ;
- we employ fits of order $d = 5, 6$ for the vacuum gauge action;
- we use two different fit ansätze for the $\bar{\psi}\psi$ renormalization;
- we employ two different sets of node points for the spline fits;
- we apply, or not, the tree level improvement to the finite- N_τ trace anomaly.

These choices give us 32 analyses which we combine with the histogram method of Ref. [69].

Integration constant

In this work we choose to calculate the integration constant for the pressure at $T_0 = 185$ MeV, to minimize the uncertainty on the equation of state in the transition region. The pressure is obtained as an integral of the renormalized chiral condensates. We performed dedicated simulations at $T_0 = 185$ MeV on lattices with $N_\tau = 8, 10, 12, 16$ and aspect ratio $LT = 4$. We start the integration from the mass of the charm quark m_c , integrate the 3-flavour theory down to the strange quark mass m_s , then integrate the two-flavour theory down to the light quark mass m_l :

$$\frac{p(T_0)}{T_0^4} = \int_{m_s}^{m_l} dm_2 \langle \bar{\psi}\psi \rangle_2(m_2) + \int_{m_c}^{m_s} dm_3 \langle \bar{\psi}\psi \rangle_3(m_3). \quad (\text{S9})$$

In the left panel of Fig. S2 we show the integrands as functions of the quark mass in the 2- (red, left) and 3- (blue, right) flavour theories, on our $48^3 \times 12$ lattice. The resulting total integral will be $2 \times$ the integral of the red curve plus $3 \times$ the integral of the blue one. We note that these data, too had to be generated for all four of our lattice spacings, and for every mass $T = 0$ simulations it was necessary to calculate the additive counterterm to $\bar{\psi}\psi$. While for $m < m_s$ these vacuum contributions could be easily interpolated (we employed a 2/2 rational function), for $m \geq m_s$ each value of m and N_τ needed a dedicated renormalization run. For $m > m_s$ we fitted the exponential of a 1/1 rational function and integrated that.

We also varied the scale setting for the integration constant. If the temperature is fixed at $T_0 = 185$ MeV, a different scale setting would require a different gauge coupling β , with new renormalization runs, etc. Instead of simulating scale setting specific, and expensive ensembles, we calculated the scale setting corrections by integrating the trace anomaly between the temperatures that belong to the simulated bare parameters with the respective scale setting. This temperature interval is N_τ dependent, thus, the continuum extrapolations have a very different slope as we switch between scale setting parameters (see right panel of Fig. S2). In the same plot we also include the extrapolation with and without tree level improvement to the finite- N_τ pressure.

The final results for the equation of state at zero chemical potential are listed in Table S1.

ENTROPY CONTOURS FOR $\mu_B \neq 0$

The calculation of the entropy contours is done in two steps. In the first step, the entropy is determined as a function of T and purely imaginary μ_B in full continuum QCD. The second step is the analytic continuation of these contours to real chemical potentials.

Calculation of entropy at purely imaginary chemical potentials

The determination of the entropy as a function of temperature and imaginary chemical potential starts by measuring the first derivative

$$\hat{n}_1 = \left(\frac{\partial(p/T^4)}{\partial(\mu_B/T)} \right)_{n_S=0}. \quad (\text{S10})$$

Note that the chemical potential derivative is taken along the direction defined by vanishing strangeness density and electric charge chemical potential $\hat{n}_1(T, \mu_B/T) = n_B(T, \mu_B)/T^3$.

T [MeV]	$p(T)/T^4$	$s(T)/T^3$	$\epsilon(T)/T^4$	$I(T)/T^4$
120	0.433(53)	2.41(25)	1.98(22)	0.69(18)
125	0.464(51)	2.68(18)	2.22(15)	0.83(13)
130	0.500(47)	2.99(18)	2.49(16)	0.99(19)
135	0.541(43)	3.34(21)	2.80(21)	1.18(23)
140	0.587(40)	3.76(23)	3.18(22)	1.42(22)
145	0.642(39)	4.30(21)	3.66(20)	1.74(19)
150	0.707(38)	4.96(16)	4.25(14)	2.14(13)
155	0.784(36)	5.69(13)	4.90(11)	2.55(11)
160	0.871(34)	6.39(14)	5.52(12)	2.91(12)
165	0.965(32)	7.05(14)	6.08(12)	3.19(13)
170	1.063(30)	7.66(14)	6.59(13)	3.40(13)
175	1.164(29)	8.23(15)	7.06(14)	3.57(14)
180	1.267(28)	8.78(17)	7.51(15)	3.71(14)
185	1.371(28)	9.32(18)	7.95(16)	3.83(14)
190	1.474(28)	9.84(19)	8.36(17)	3.93(14)
195	1.578(29)	10.32(21)	8.74(19)	4.00(16)
200	1.680(30)	10.77(23)	9.09(21)	4.04(16)
205	1.780(32)	11.17(24)	9.39(22)	4.05(16)
210	1.878(33)	11.53(24)	9.65(22)	4.02(15)
215	1.972(35)	11.86(24)	9.89(21)	3.97(14)
220	2.062(36)	12.16(25)	10.10(22)	3.91(14)
225	2.150(38)	12.45(25)	10.30(22)	3.85(14)
230	2.234(39)	12.72(26)	10.49(23)	3.79(14)
235	2.315(41)	12.99(27)	10.67(23)	3.73(14)
240	2.392(42)	13.24(27)	10.85(23)	3.67(14)
245	2.467(44)	13.48(28)	11.01(24)	3.61(13)
250	2.540(46)	13.71(29)	11.17(24)	3.55(13)
255	2.609(47)	13.93(29)	11.32(25)	3.50(13)
260	2.675(49)	14.14(30)	11.46(25)	3.44(13)
265	2.740(51)	14.34(31)	11.60(26)	3.38(13)
270	2.803(53)	14.54(31)	11.74(26)	3.33(13)
275	2.863(54)	14.73(32)	11.86(27)	3.27(12)
280	2.922(56)	14.91(33)	11.99(27)	3.22(13)
285	2.978(58)	15.08(34)	12.10(28)	3.17(14)
290	3.033(59)	15.25(35)	12.21(30)	3.11(15)
295	3.086(61)	15.40(37)	12.32(32)	3.06(18)

TABLE S1. The tabulated equation of state at zero chemical potential: pressure, entropy density, energy density and trace anomaly.

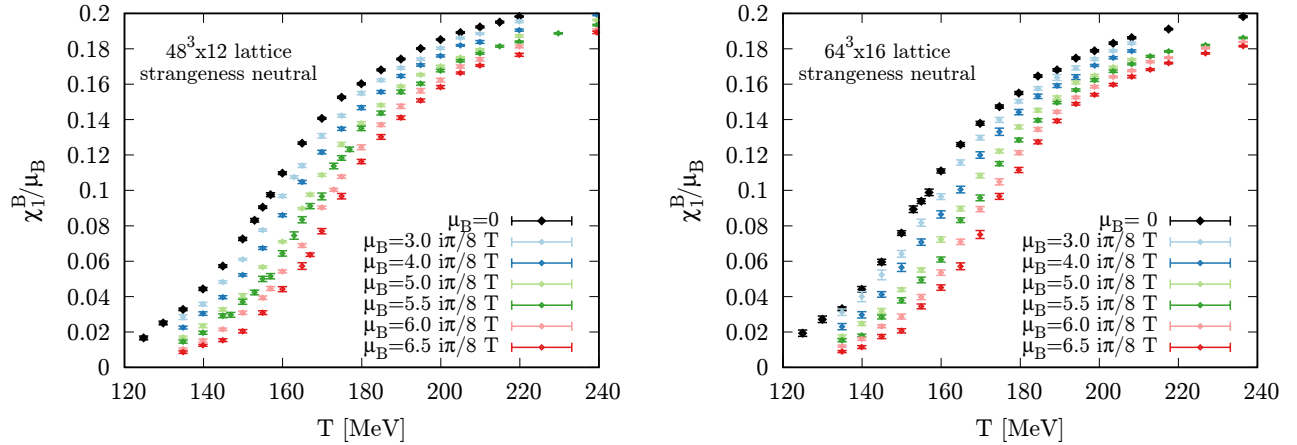


FIG. S3. Lattice data of $\hat{n}_1(T)/\hat{\mu}_B$ as a function of the temperature for the simulated imaginary (and zero) values of chemical potentials. We show the data on our two finest lattices: $48^3 \times 12$ and $64^3 \times 16$.

In Fig. S3 we show the raw input data as obtained from the simulations, for our two finest lattices. We generated 4000 configurations per ensemble. For this work we generated a data set at $\mu_B/T = 5.5i\pi/8$ on the $40^3 \times 10$ lattice, and at $\mu_B/T = (5.5, 6 \text{ and } 6.5)i\pi/8$ on the $64^3 \times 16$ lattice. On the $48^3 \times 12$ lattice, all these were already available and used e.g. in Refs. [3, 25].

Within each ensemble we computed \hat{n}_1 , the strangeness density as well the μ_S -derivative of both. The parameters were previously tuned such that the strange expectation value approximately vanishes. We used the μ_S derivatives to extrapolate \hat{n}_1 to exactly vanishing strangeness. Tuning to strangeness neutrality was discussed in more detail in Refs. [3, 25].

After the calculation of \hat{n}_1 we utilize the following thermodynamics relations:

$$s(T, \mu_B) = \left(\frac{\partial p}{\partial T} \right)_{\mu_S}, \quad p(T, \mu_B) = \int_0^{\mu_B} n_B(T, \mu'_B) d\mu'_B, \quad (\text{S11})$$

where p is the pressure. Converting derivatives at fixed μ_B to derivatives at fixed $\hat{\mu}_B = \mu_B/T$ we get [24]:

$$\hat{s}(T, \hat{\mu}_B) - \hat{s}(T, 0) = 4(\hat{p}(T, \hat{\mu}_B) - \hat{p}(T, 0)) + \left(\frac{\partial \hat{p}(T, \hat{\mu}_B)}{\partial T} - \frac{\partial \hat{p}(T, 0)}{\partial T} \right) - \hat{\mu}_B \hat{n}_1, \quad (\text{S12})$$

where the dimensionless pressure is $\hat{p} = p/T^4$ and the dimensionless entropy is $\hat{s} = s/T^3$. In order to perform the T derivatives and μ_B integrals needed for the calculation of the entropy, as well as for the continuum limit extrapolation, we fit \hat{n}_1 with the following linear ansatz:

$$\hat{n}_1(T, \hat{\mu}_B) = \sum_{klm} c_{klm} f_k(T) g_l(\hat{\mu}_B) h_m(N_t), \quad (\text{S13})$$

where the c_{klm} are fitted real parameters, while the $f_k(T)$, $g_l(\hat{\mu}_B)$ and $h_m(N_t)$ are fixed basis functions in the T , $\hat{\mu}_B$ and N_t directions respectively. By exactly differentiating the basis function $f_k(T)$ and exactly integrating the basis functions $g_l(\hat{\mu}_B)$ the different terms in equation (S12) can be obtained. For the different basis functions in the N_t direction we choose $h_0 = 1$, $h_1 = 1/N_t^2$. Thus, we perform a linear continuum extrapolation in $1/N_t^2$. Note that we always include a tree level correction in the observable \hat{n}_1 . In the chemical potential direction we have 2 different choices of the basis functions:

1. $g_0 = 1$, $g_1 = \hat{\mu}^2$, $g_2 = \hat{\mu}^4$, $g_3 = \hat{\mu}^6$, and
2. $g_0 = 1$, $g_1 = \hat{\mu}^2$, $g_2 = \hat{\mu}^4$, $g_3 = \hat{\mu}^6$, $g_4 = \hat{\mu}^8$.

In the T direction we use cubic splines, with fixed node points at several temperatures. To estimate the systematics of this temperature interpolation we use 4 different choices for the node points:

1. [129, 142, 152, 162, 172, 182, 192, 202, 222, 251] MeV,
2. [129, 145, 155, 165, 175, 185, 195, 205, 225, 251] MeV,
3. [129, 139, 148, 158, 168, 178, 188, 198, 218, 238, 251] MeV and
4. [129, 144, 159, 174, 189, 204, 219, 234, 251] MeV.

Another source of systematic errors that is taken into account at this point are 2 different choices for the scale setting: either the pion decay constant f_π or the Wilson flow scale w_0 introduced in Ref. [73].

Finally, the finite chemical potential contribution of Eq. (S12) is added to the $\mu_B = 0$ contribution, and the results are then utilized for the final step of this analysis, the analytic continuation step.

Entropy contours

The entropy contours are modeled as 1/1 rational functions in μ_B^2 . Data points at different imaginary μ_B are correlated, since the entropy itself is a result of an integration in imaginary μ_B . If the p -value of the correlated fit is below a cut (0.02), we drop that T_0 value from the analysis.

For a fixed, positive μ_B^2 parameter we consider several contours, defined by the axis intercept T_0 in 1 MeV steps in the range 131...180 MeV. The T_s contour value as a function of T_0 is the basis of the further analysis.

This $T_s(\mu_B^2, T_0)$ function is available to us numerically with jackknife errors. Whether the entropy is multi-valued at a given point, is determined on the basis of the $\partial T_s/\partial T_0$ derivative. This requires some level of interpolation. We use fourth degree polynomials to find the derivatives. We perform fully correlated fits to the data points.

As systematics we vary the following options:

- the upper range of the fit $T_{0,\max} = 161$ or 170 MeV;
- the lower range of the fit $T_{0,\max} = 130$ or 135 MeV;
- we sample T_0 every 2,3 or 4 MeV

For the full analysis, more than 16000 such fits are performed if we count all μ_B values, where we step in 10 MeV units. 49.3 % of the fits have a p -value better than 0.5.

We work through the temperatures in the phase diagram in 2 MeV steps. For each selected T we solve $T_s(\mu_B^2, T_0) = T$, thus arriving at a T_0 value with some statistical error. This error is propagated to $\partial T_s/\partial T_0$.

Since all considered fits were acceptable, we use uniform weighting when we combine the analyses. In practice, we average Gaussian cumulative distribution functions defined by the central sample and the jackknife error of $\partial T_s/\partial T_0$. The resulting distribution allows us to identify those positions in the phase diagram where the derivative is inconsistent with zero or negative values with a confidence level that would correspond to 2σ for a Gaussian distribution.